Boundary Effects in the Eigenstrain Method

Lee, S-Y, Coratella, S, Brügger, A, Clausen, B, Brown, D, Langer, K, Fitzpatrick, M & Noyan, IC

DOI 10.1007/s11340-018-0378-3
ISSN 0014-4851
ESSN 1741-2765
Publisher: Springer

Boundary Effects in the Eigenstrain Method

Seung-Yub Lee[1], Stefano Coratella[2], Adrian Brügger[3], Bjørn Clausen[4], Donald Brown[4], Kristina Langer[5], Michael E. Fitzpatrick[6], I.C. Noyan[1,*]

[1]*Applied Physics and Applied Mathematics, Columbia University, New York, NY 10027, USA*
[2]*Aerospace Mechanics Division, University of Dayton Research Institute, Dayton, OH 45409, USA*
[3]*Civil Engineering and Engineering Mechanics, Columbia University, New York, NY 10027, USA*
[4]*MST-8, Los Alamos National Laboratory, Los Alamos, NM 87545, USA*
[5]*Air Force Research Laboratory, ARFL/RQVS, Wright-Patterson AFB, OH 45433, USA*
[6]*Faculty of Engineering and Computing, Coventry University, Gulson Rd, Coventry CV1 2JH, United Kingdom*

Abstract We present a comprehensive study of the effects of internal boundaries on the accuracy of residual stress values obtained from the eigenstrain method. In the experimental part of this effort, a composite specimen, consisting of an aluminum cylinder sandwiched between steel cylinders of the same diameter, was uniformly heated under axial displacement constraint. During the experiment, the sample temperature and the reaction stresses in the load frame in response to changes in sample temperature were monitored. In addition, the local (elastic) lattice strain distribution within the specimen was measured using neutron diffraction. The eigenstrain method, utilizing finite element modeling, was then used to predict the stress field existing within the sample in response to the constraint imposed by the load frame against axial thermal expansion. Our comparison of the computed and measured stress distributions showed that, while the eigenstrain method predicted acceptable stress values away from the cylinder interfaces, its predictions did not match experimentally measured values near them. These observations indicate that the eigenstrain method is not valid for sample geometries with this type of internal boundaries.

Keywords Eigenstrain, Residual Stress, Neutron Diffraction. Finite Element Analysis, Mechanical Constraint, Boundary Condition

Introduction

The term *eigenstrain* was introduced by Mura in 1987 [1] in micromechanical analysis of the origins of residual stress fields[1]. In current usage this term encompasses all inelastic strains, such as strains resulting from thermal expansion, purely plastic flow, phase transformations and/or compositional changes resulting in changes of the specific volumes of transformed regions. Such *inelastic strains* were first discussed by Reissner in 1931 [2] to describe misfit strains. Subsequently, Eshelby defined the term *stress-free transformation strain* in the computation of the elastic strain field within an ellipsoidal inclusion embedded in a matrix material (Eshelby, 1957, 1959) [3, 4]. We use a simpler definition of eigenstrain which is based on elastic energy considerations. We note that, irrespective of their origin, eigenstrains, themselves, do not cause elastic energy storage in the atomic bonds of the body. Residual stresses, which indicate elastic energy storage in atomic bonds, arise within the body in response to external and/or internal constraint of the regions where eigenstrains are induced. If the final eigenstrain distribution is homogeneous at all points within the volume of an unconstrained body, the body dimension changes, but the body remains residual-stress-free; no elastic energy is stored in its atomic bonds.

The "*eigenstrain method for determining residual stresses*" (eigenstrain method) was proposed to compute residual stresses which arise in response to eigenstrain distributions within a solid sample. In this formalism the eigenstrains used for the computation are estimated from residual stresses measured in test coupons, usually with simple geometries, which have been subjected to the same manufacturing process as the component of interest. The residual stresses in the actual component are, then, obtained by utilizing these inelastic strains in a finite-element model incorporating the boundary conditions of the component. The major advantage claimed for this approach is the ability to calculate the entire residual stress field within an actual engineering component from a limited set of residual stress data. This approach was first proposed by Fujimoto in 1970 [5] using the term *inherent strain*. A method to calculate the eigenstrain was not provided. In 1975, Ueda and co-workers [6] published the first complete application of the modern eigenstrain approach and calculated the total residual stress profile

[1] The term "eigenstrain" stems from the word "*eigen*" in German which means "inherent, particular, characteristic or peculiar". Thus, the term "eigenstrain" can also be termed "inherent strain". Eigenstrain is not related to eigenvalues or eigenvectors commonly encountered in physical and mathematical analysis. In German literature residual stresses are termed "*Eigenspannungen*" [2].

within a welded plate through finite element analysis. An improved version of Ueda's technique was proposed by Hill (Hill *et al*., 1995, 1998) [7, 8] to obtain all three axial residual stress components in long welded joints; this method is limited to joints with simple geometries.

With the advent of faster, more reliable, and cost-effective, computer–aided finite element techniques, the eigenstrain method has been extensively used to predict the residual stress fields in different applications such as friction stir welding (Luckhoo *et al.*, 2009; Jun *et al.*, 2010) [9, 10], shot peening (Korsunsky, 2005; Jun *et al.*, 2011; Song *et al.*, 2012) [11-13], and laser shock peening (Korsunsky, 2006; Achintha & Nowell, 2011; Hu & Grandhi, 2012; Achintha *et al.*, 2013; Correa *et al.*, 2015; Coratella *et al.*, 2015) [14-19]. In 2010, Jun and Korsunsky [20] proposed the SIMple TRIangle method (SIMTRI) to implement the Eigenstrain Reconstruction Method (ERM) within the finite element modelling framework and demonstrated its versatility on a variety of problems.

Despite the popularity of the eigenstrain method for computing stress values, its limitations have not been systematically examined in the literature. There was only a single article where the uniqueness of the eigenstrain formalism was formally discussed (Luzin, 2014) [21], where it was shown that, since the eigenstrain method involves the solution of inverse elasticity problems, its capability to uniquely predict residual stress tensor distributions is limited to simple component geometries with simple material and eigenstrain distributions. We were not able to find any articles which presented a rigorous analysis of the uncertainty associated with the eigenstrain formalism. To estimate the accuracy, one needs to know the actual values of eigenstrains, and corresponding residual stress distributions, within the actual component. This is a hard task in samples with complex geometries and heterogeneous distributions of physical properties. In addition, because of the multiple steps associated with the analysis and the complexity of the computations involved, propagation of error terms to estimate the uncertainty associated with the stress values obtained from the eigenstrain analysis is non-trivial. It is possible, however, to design samples which can yield some insight. In what follows we present the design and implementation of a simple thermo-mechanical test which can be used to quantify the uncertainties associated with the eigenstrain analysis.

Experimental Details

Experiment Design and Samples

The following steps are used in a typical application of the eigenstrain method:

1- A proof sample with the same material properties as the component of interest, but with a much simpler geometry, is treated with the same manufacturing process to which the component of interest has been subjected. For example, a simple strip is shot-peened with the parameters of interest (Figure 1 (a)).

2- Residual stresses are measured experimentally from the proof sample. For the strip in Fig. 1 (a), one can use diffraction (Noyan & Cohen, 1985, 1987) [22, 23], hole-drilling (Schajer 1988, 1988) [24, 25], contour methods (Prime, 2001; Prime *et al.*, 2006) [26, 27], or combined techniques (Schajer, 2010; Woo *et al.*, 2013) [28, 29] for this purpose.

3- FEM analysis is used to reconstruct the depth-dependent eigenstrain profile, $\varepsilon_{ij}^{*}(z)$, in the proof sample which would result in the measured residual stresses.

4- The calculated eigenstrain field, $\varepsilon_{ij}^{*}(z)$, of the proof sample is used to model the residual stresses expected in the component of interest. For this purpose, numerical methods, such as finite element or finite-difference based formalisms, are used. Based on the "Principle of Transferability of Eigenstrain" (Jun *et al.*, 2011) [12], $\varepsilon_{ij}^{*}(z)$ obtained from the proof sample is expected to enable the computation of accurate residual stress fields for different component geometries (Figure 1 (b), (c), (d)), regardless of location (center or edge) or shape (flat or round) of the peened domains.

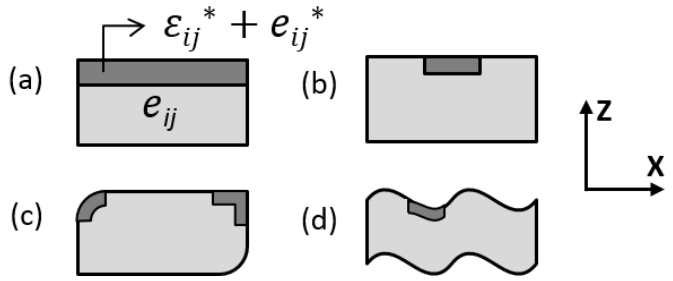

Fig. 1 Schematic diagram of a proof specimen (a) for eigenstrain analysis after shot-peening. Once the eigenstrains, $\boldsymbol{\varepsilon_{ij}^{*}(z)}$, in (a) are computed from measured elastic strains, $\boldsymbol{e_{ij}^{*}}$, the residual stresses in components with identical material properties, peened with identical parameters but with different geometries, (b) ~ (d), can be computed.

For verification and validation of this formalism, two basic questions need to be addressed. First, is the eigenstrain profile computed from the residual stress distribution of the proof sample unique and correct? Second, given the exact eigenstrain distribution in the proof sample, can we calculate accurate stress profiles in other samples regardless of geometry? Luzin [21] has published a rigorous theoretical analysis of the first problem, where he showed that unique and tractable solutions can only be obtained for simple geometries such as plates, spheres and cylinders, when the eigenstrain distributions, also, have simple functional forms. Consequently, we limited our investigation to one such geometry and re-formulated the second question: we can measure the exact thermal strain distributions (eigenstrains) within the components of an axially piecewise homogeneous composite cylinder caused by a temperature increase, ΔT, without external constraint. Can we, then, determine the residual stresses within the composite using the eigenstrain method when the composite sample boundaries are constrained during the heating step? This formulation fits the four steps of the traditional eigenstrain analysis listed above, and satisfies the uniqueness conditions discussed by Luzin, if:

1- All cylinders have the same diameter.
2- There is no axial temperature gradient within the sample.
3- All cylinder materials have cubic symmetry and, thus, have isotropic linear thermal expansion coefficients.
4- There is no plastic flow, creep, or phase transformations in any of the cylinders in response to heating in the constrained state.

Figure 2 shows the actual implementation of our design. We manufactured a composite cylinder, ½" (12.7 mm) in diameter, where a 1.25" (31.8 mm) long, 6061 aluminum cylinder was sandwiched between two, 2" (50.8 mm) long, 1018 low carbon steel cylinders. The other ends of the steel cylinders were fitted into 6061 Al spacers which served as axial alignment fixtures and heater blocks; these could be heated independently through 500W Watlow clamp heaters, each connected to an independent channel of a Lakeshore 336 multi-channel temperature controller. Two machinable-ceramic (MACOR) cylinders, also nominally ½" (12.7 mm) in diameter, isolated the Al heater sleeves from the (cooled) grips of the horizontal Instron hydraulic load frame, which was mounted on the SMARTS engineering neutron diffractometer at the Lujan Center of Los Alamos National Laboratory.

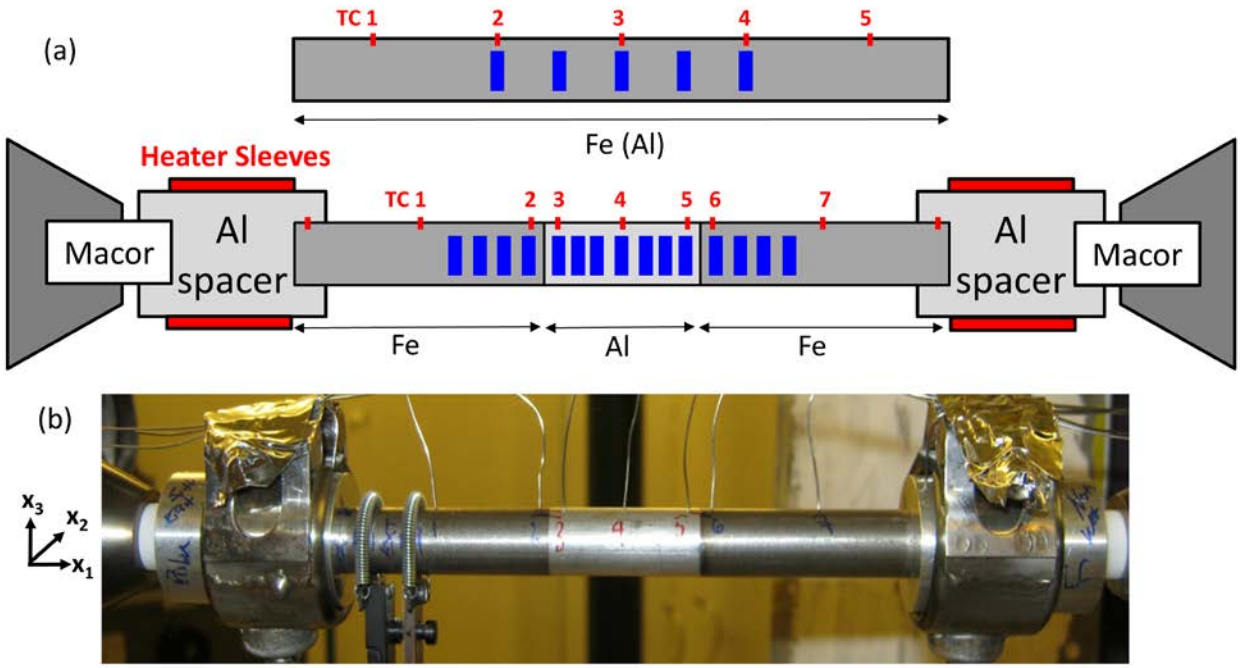

Fig. 2 (a) Schematic of the experimental geometry both proof (top) and composite cylinders are shown. Volumes interrogated by neutrons are shaded by blue rectangles. Thermocouple locations, TC1~TC7 are also marked. Bottom picture (b) shows the composite sample loaded in the load frame.

Table 1 Mechanical and thermal properties of the components along the loading axis. The mechanical parameters of steel, and aluminum were obtained from the Metals Handbook[2] [30, 31]. The MACOR data were supplied by the manufacturer (Corning Inc.). These values are also available in MatWeb [32].

	Young's modulus E / GPa	Poisson's ratio ν	Shear modulus, G / GPa	Yield stress σ_y / MPa	Room-temperature CTE / 10^{-6}	Thermal conductivity κ / W mK^{-1}
Carbon Steel 1018 [30]	200	0.29	78	~ 370 (tensile)	12.5	52
Aluminum Alloy 6061 [31]	69	0.33	26	~ 270 (tensile)	23.6	167
MACOR Ceramic [32]	67	0.29	26	~ 345 (compressive)	9.3	1.46
Virtual Grips (Model only)	20	0.33	NA	NA	NA	NA

[2] We also measured mechanical parameters at room temperature, and CTE values, in the RT-100 ˚C range for the steel and Al cylinders. All values agree within experimental error.

The axial temperature distribution in the composite was monitored with seven type-K thermocouples. Each Al spacer had an independent control thermocouple. For CTE and compliance measurements, two proof samples were used: these were 5.25” (133.4 mm) long, single piece, 6061 aluminum (Al) and 1018 steel cylinders, ½” (12.7 mm) in diameter. Mechanical and thermal properties of the parts along the loading axis are listed in the Table 1.

Neutron Diffraction Measurements

In situ neutron diffraction measurements were performed on the Spectrometer for Materials Research at Temperature and Stress (SMARTS) beam line at Los Alamos Neutron Science Center (LANSCE) to determine lattice strains during thermal and/or mechanical loading experiments. The experimental geometry is shown in Figure 3. The cylinder loading axis (‘x_1’) is oriented at 45° to the incident neutron beam, so that Bank 1 (East) and Bank 2 (West) detectors record diffraction signals from atomic planes normal to the x_2 and x_1, directions of the cylindrical samples, respectively. We note that, due to the cylindrical symmetry of the samples the orthogonal coordinates defining the base plane of the cylinder, x_2 and x_3, are indistinguishable.

The beam size was confined by setting the incident beam slit dimensions to 2×8 mm^2, and placing 2 mm acceptance-length radial collimators in front of both detectors. These settings defined an illuminated volume in the shape of an elongated cuboid, with edge dimensions of approximately $2.8 \times 2.8 \times 8$ mm^3 along the x_1, x_2 and x_3 directions respectively. During measurements careful sample positioning, utilizing step-scanning of the sample while monitoring the relevant diffraction peaks, ensured that the entire illuminated volume (information volume) was completely contained within either steel or Al cylinders, as needed (Noyan *et al.*, 2010) [33].

During neutron measurements all samples, composite or proof, were first placed in the load frame at room temperature (20˚C), and then loaded in compression to –15 MPa (in load control) to eliminate any play in the load train[3]. The samples were then aligned with respect to the neutron beam. For the proof specimens, 5.25”-long (133.4 mm) single piece Al and steel cylinders, modulus verification measurements were performed by mechanical loading at room temperature. The CTE values were determined from the variation of the lattice parameter with

[3] During the loading operation, the composite sample was contained in an axially split Al tube, ½” (12.6 mm) inner diameter and 4” (101.6 mm) in length, to keep all three cylinders in alignment. After the ends of the outer steel cylinders were captured in the Al spacers, the sample was loaded in compression and the alignment tube was removed. After this point the sample was kept together by the applied compressive load and friction at the cylinder surfaces.

temperature while the samples were under load control at –15 MPa.

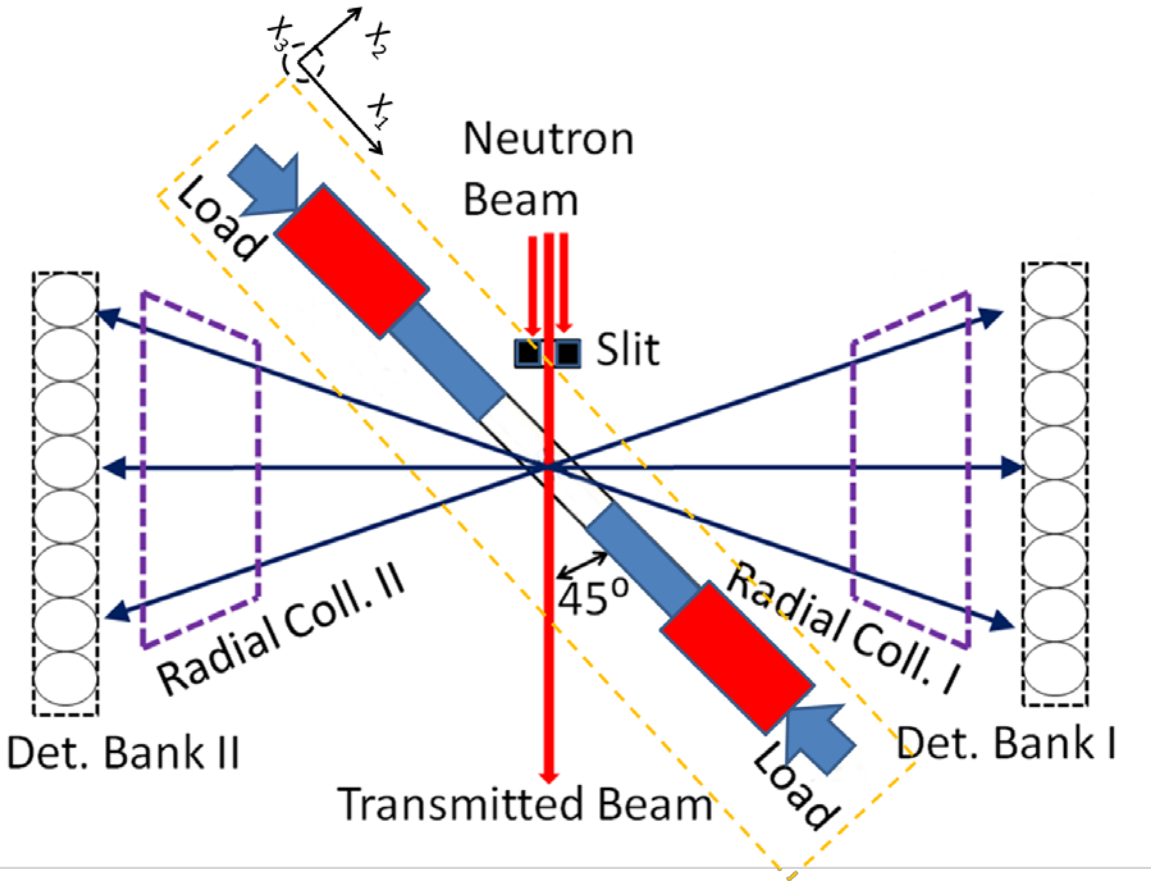

Fig. 3 Schematic (top view) of the neutron diffraction experiment. The load frame is installed on a precision table (rectangle with dashed lines), and can be moved along the x_1, x_2 and x_3 coordinates to position any volume within the (loaded) specimen in the neutron information volume.

For strain measurements at temperature, the following steps were carried out for all samples. First, the sample was slowly heated to the set-point temperature (60 or 100˚C). After the sample temperature stabilized, position-dependent diffraction measurements were performed to measure the lattice strain distribution along the cylinder axis. In case of CTE measurements, the proof specimens were heated while the system was under load control at –15 MPa and lattice strains were measured at five equidistant locations over the central 3” of each specimen.

During constrained thermal expansion measurements, the composite sample was first loaded in compression to –15 MPa at room temperature, and then the load frame was switched to displacement control and the crosshead position was fixed for the duration of the experiment. During heating to the set-point temperature, the reaction stress values imposed by the load frame to keep the crosshead position invariant were recorded. Once all temperatures, as read from the

thermocouple reader, stabilized to $\pm 1^{\circ}$C, lattice strains at 15 positions, 7 in the Al cylinder and 4 in each steel cylinder, were measured. These locations are marked with blue rectangles in Fig.2. The measurement locations bracketing the steel-aluminum interfaces required careful alignment to ensure that the diffracting volume (gage volume) was completely contained in only one kind of material[4].

Figure 4 shows the variation of temperatures determined from the thermocouples as a function of position (Fig. 4 (a)) and time (Fig. 4 (b)). The thermocouple locations correspond to those indicated in Fig. 2. These figures show that, even though the set-points of the heaters were identical, small, non-symmetric, temperature gradients existed over the composite sample. The asymmetry was more pronounced on the right side relative to Fig. 2. We attribute this asymmetry to the slightly different thermal resistance of the aluminum-steel interface on that side (Lee *et al.*, 2014) [34]. We observed that the magnitude of the temperature gradient increased with increasing temperature, reaching approximately 8˚C between thermocouples 5 and 7 when both controllers were set for 100˚C. Computations indicated that the effect of such a gradient was minimal, so the measurements were carried out with this thermal gradient in the sample, instead of manipulating the individual controllers to achieve a flat temperature profile and wasting beam time in the process.

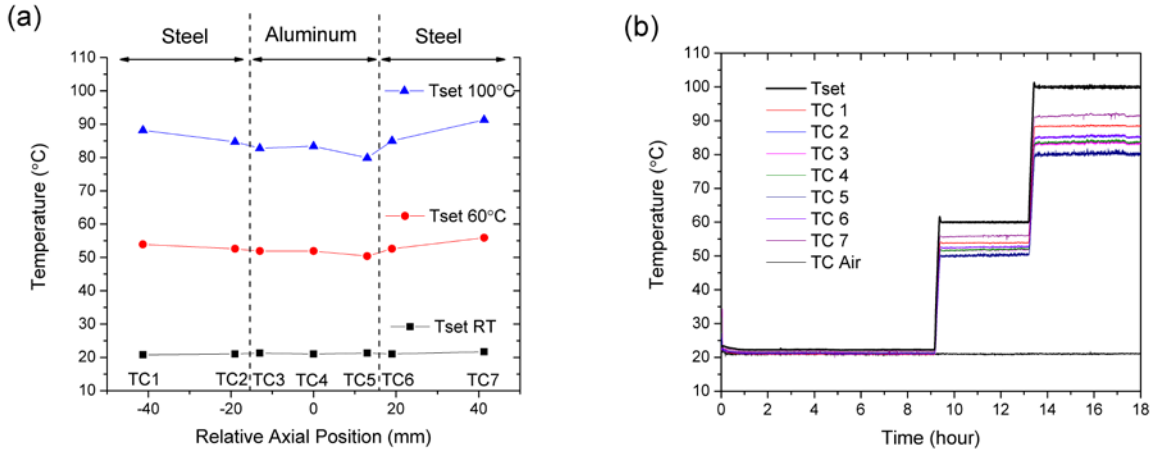

Fig. 4 (a) Axial variation of temperature in the composite sample at three set-points. The time stability of temperature profiles in the samples during the measurement sequence is shown in (b). Thermocouple locations correspond to those shown in Fig. 2.

[4] This was ensured by monitoring the diffraction spectra as the beam position was stepped over the interface. The chosen locations, bracketing the respective interfaces at ±3 mm, yielded only Al or Fe spectra to avoid partially-buried gage-volumes; these cause large errors in the measured strain values (Spooner & Wang, 1997) [35].

Figure 5 shows representative diffraction patterns from the Al and steel cylinders. All patterns were analyzed using the public-domain GSAS Rietveld refinement package (Von Dreele *et al*., 1982) [36] implemented through the SMARTSware-program (Clausen, 2004) [37] which permitted consecutive refinement and lattice parameter export. Lattice parameters in axial (a_1) and transverse (a_2) directions were obtained at all locations. For the counting times utilized, the average fitting uncertainty of Fe and Al patterns were 20-25 με and 30-40 με, corresponding to stress uncertainties of ± 4-5 MPa and ± 2-3 MPa, respectively.

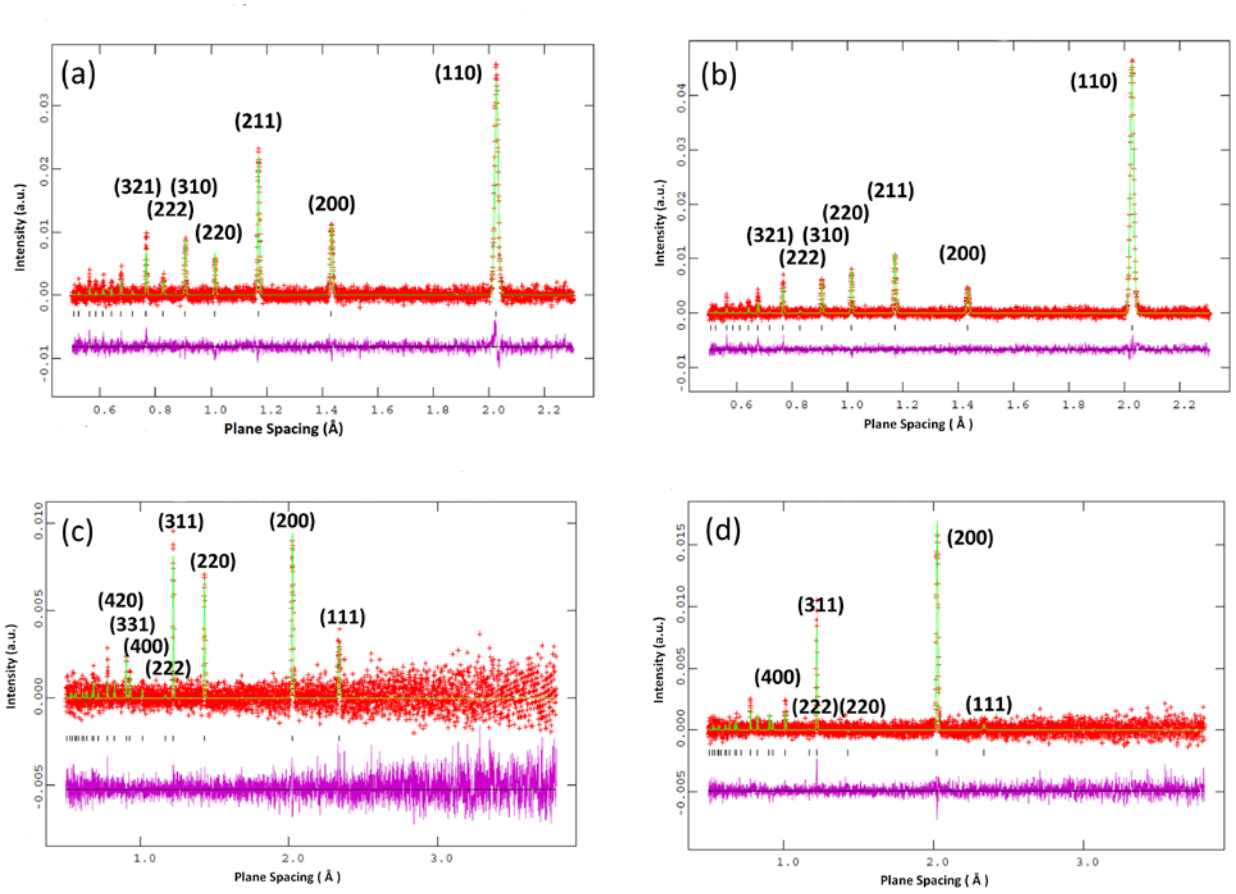

Fig. 5 Typical spallation neutron spectra in detector banks 1 and 2 from the steel (a, b) and aluminum cylinders (c, d) of the composite specimen. The indexed Bragg peaks were used for the GSAS analysis. For all figures the residual between the experimental data and the GSAS model is also included. The data indicate the presence of texture for both materials. Texture is more pronounced for the Al cylinder.

Analysis Procedure

Basic Strain Analysis

In our experiments the total normal lattice strains, ε_{ii}, were obtained from measured axial and transverse lattice parameters a_1, a_2, using:

$$\varepsilon_{ii} = \frac{a_i - a_{0,i}}{a_{0,i}} \quad (1)$$

Here $a_{0,i}$ is the "unstressed lattice spacing" of the material for the axial, x_1, and transverse, x_2 , directions, respectively. For each location, the lattice parameters, $a_{0,1}$, $a_{0,2}$, obtained from room temperature data at –15 MPa compressive load at that particular location were utilized as the reference lattice parameter. This approach sets the "zero strain" state of the material as the first set of data points, and removes contributions from any pre-existing residual stress fields and/or intergranular strains from the subsequent analysis (Mei *et al*., 2013) [38]. Since the orthogonal transverse axes in our sample geometry, $x_2, x_3,$ are indistinguishable, we did not measure the lattice spacing, a_3, and compute the normal strain ε_{33}, but assumed that the transverse strains were equal, $\varepsilon_{22}=\varepsilon_{33}$. This assumption is based on our measurements in other cylindrical specimens under uniaxial loading (Brügger *et al*., 2017) [39]. In addition, the validity of this assumption was verified in our current FEM models.

The strains ε_{ii} measured during the thermo-mechanical steps of the experiment can have contributions from: 1) any expansion or contraction of the crystalline lattice caused by changes in temperature, ${\varepsilon_{ii}}^{th}$; and 2) the elastic lattice strain terms, e_{ii}, that form in response to any constraints which prevent the material from achieving its equilibrium lattice spacing at the specific temperature[5]:

[5] For brevity this discussion assumes a uniformly heated crystalline material with isotropic thermal and mechanical properties, in which all eigenstrain terms, except thermal strains, are zero.

$$\varepsilon_{ii} = {\varepsilon_{ii}}^{th} + e_{ii} \quad (2)$$

The (unconstrained) thermal strain (eigenstrain) is obtained by integration of the coefficient of thermal expansion of the material, $\alpha(T)$, over the corresponding temperature range:

$${\varepsilon_{ii}}^{th} = \int_{T_1}^{T_2} \alpha(T) dT \quad (3\text{-a})$$

If the CTE can be considered constant over this temperature range,

$${\varepsilon_{ii}}^{th} = \alpha\, \Delta T \quad (3\text{-b})$$

For our system, where all materials have cubic crystal symmetry, the elastic constraint strain terms along the axial and transverse directions at a given point are given by:

$$e_{ii} = \varepsilon_{ii} - {\varepsilon_{11}}^{th} \quad (4)$$

Using the symmetry of the system we obtain:

$$e_{11} = \varepsilon_{11} - {\varepsilon_{11}}^{th} \quad (4\text{-a})$$

$$e_{22} = e_{33} = \varepsilon_{22} - {\varepsilon_{11}}^{th} \quad (4\text{-b})$$

To aid the elastic analysis we define a "boundary constraint factor", B_c:

$$B_c = \frac{\nu e_{11} + e_{22}}{(1+\nu)} = \frac{\nu \varepsilon_{11} + \varepsilon_{22}}{(1+\nu)} - \alpha\, \Delta T \quad (5)$$

If the uniaxial macroscopic boundary constraint applied by the load frame to the sample along its axis is also valid in a particular local domain, the corresponding axial and radial constraint terms will be related through Poisson's ratio, υ : $e_{22} = -\upsilon e_{11}$, and the term, B_c , will be zero.

Once the expected thermal strain has been computed from tabulated or experimentally determined CTE values, Equations (4) and (5) provide simple checks of the strain state of the domain in which the axial and transverse lattice strains have been measured. Three cases of interest can be identified[6]:

1- If the measured strains, ε_{ii}, are equal to the thermal strain computed from Eqtn. (3-a), then the system is exhibiting unconstrained thermal expansion, and the lattice strains

[6] We note that, in the case of an isothermal uniaxial compression test, the temperature change ΔT is zero, and the boundary constraint term, B_c, obtained from Eqtn. (5) would also be zero as long as there are no additional constraints imposed by buried interfaces.

have only thermal eigenstrain terms ($e_{11} = 0$). In this case, $B_c \equiv 0$.

2- If the elastic strains due to constraint, e_{ii}, are finite, and $B_c = 0$, the constraint imposed on the thermal expansion of the local region is along the axial direction only.
3- If both the elastic strain terms due to constraint, e_{ii}, and the boundary constraint term, B_c, are finite, constrained thermal expansion is occurring in the local volume. However, the local constraint is not equivalent to the far-field uniaxial constraint. In such a case the simple analytical formulation discussed above is no longer applicable and finite element analysis must be used to investigate the strain/stress state within the system.

Finite Element Modelling

Numerical analysis, using the ABAQUS 6.14 finite element program, was used to model the expected thermo-elastic response of the samples. An extended model was constructed which included, in addition to the specimen, idealized representations of parts of the load train of the mechanical tester. This was necessary to properly account for the compliance of the system: even though the mechanical tester was used under displacement control to eliminate any sample displacement along the axial, $(\vec{x})$, direction, the actual point at which the displacement was monitored was within the actuator assembly of the tester. Thus, the displacement which was constrained included contributions from multiple elements of the load train (Figure 6 (a)).
To include this constraint profile in our finite element model, we constructed two virtual grips bracketing the sample (each with one end fixed) which combined these contributions (Fig. 6 (b)). The modulus for these virtual grips, E_{VG}, was experimentally determined through isothermal compression tests with each type of sample. For the Young's modulus we obtained, $E_{VG} = 20$ GPa, which is significantly more compliant than any load train component. This is caused by the relatively compliant configuration of the load frame; a c-clamp type setup with a strong-back that carries the load in bending and not in tension/compression as in a typical symmetric two-column load frame.

All material properties used in the finite element model are listed in Table 1. The 3D stress element, C3D20 (20-node quadratic brick) was used for all components. Several mesh sizes were tested to eliminate mesh-size dependency of simulation results. A fine mesh size, 0.1 mm, was used within ~ ±6.5 mm of the interfaces to capture the details of any large strain gradients due to

radial and axial constraint. The mesh size within the central 18 mm of the Al cylinder was 1.2 mm. The thermal expansion was input by a pre-defined field module. This approach was adequate since no heat transfer simulations were necessary. Given the small temperature variation measured within each part (Fig. 4 (a)), only a single, uniform, (average) temperature was used in the model. This assumption did not result in any significant error in the computations.

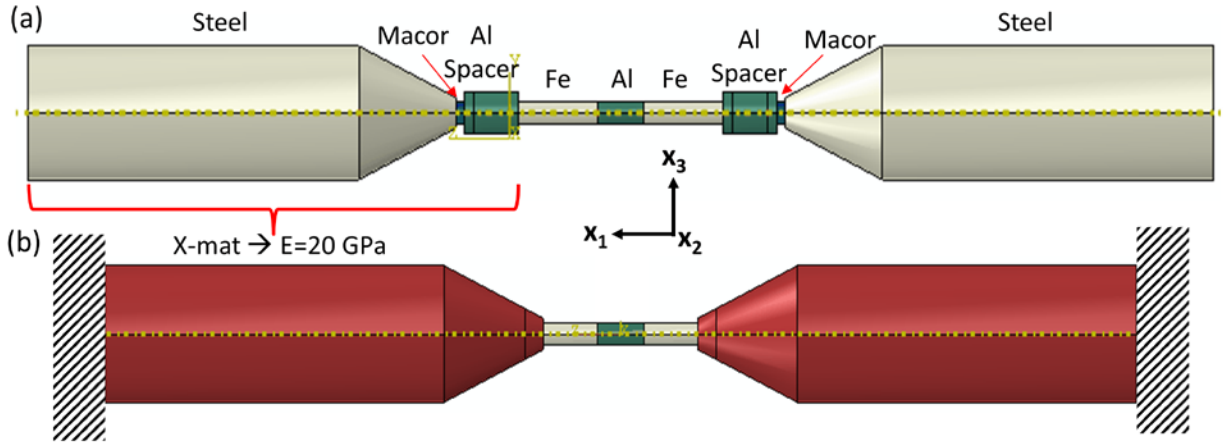

Fig. 6 Schematic (side-view) diagrams of (a) original assembly and (b) simplified finite element model.

Experimental and Modelling Results

Formalism Verification and Uncertainty Analysis

The room-temperature elastic moduli, $\partial\sigma_{app}/\partial\varepsilon$, of the steel and aluminum cylinders were determined by correlating neutron strains with applied (compressive) loads, and by traditional uniaxial compression tests. The results were consistent and showed excellent agreement with tabulated values (Table 1), with $E_{\mathrm{Fe}} = 204 \pm 15$ GPa and $E_{\mathrm{Al}} = 70 \pm 5$ GPa. Experimentally determined Poisson's ratios also agreed with literature values within experimental error.

Figure 7 (a) is a composite plot, obtained by combining five plots, each depicting the variation of the measured axial and transverse thermal lattice strains, $\varepsilon_{11}, \varepsilon_{22}$, along the axis of the 5.25" long (133.4 mm) solid steel cylinder (the proof sample), at a given set-point

temperature under –15 MPa constant load. The center of the cylinder for each set point is marked on the abscissa. The average sample temperature for each set-point, obtained from the average of all sample thermocouple readouts, is shown on the right ordinate. At room temperature the thermal strains calculated from Equation (1) at all five locations are identically equal to zero since the lattice spacings at each location measured at this temperature were used as the unstressed lattice parameter, $a_{0,i}$. No statistically significant strain gradients are observed within the proof sample at any temperature. The overall standard deviation of all thermal strains in this plot is $\pm$ 30 με.

Figure 7 (b) shows the variation of the average axial and transverse thermal lattice strains, $\varepsilon_{11}, \varepsilon_{22}$, with average sample temperature. Within statistical error, a linear variation is adequate to describe the trend. The slope of the regression line fit to the data, 12.5 ± 0.5 με/°C , agrees with in-house dilatometry measurements (12.3 ± 0.3 με/°C).

The composite Figure 7 (c) depicts the variation of the axial and transverse interaction strains, e_{11}, e_{22}, at each measurement location within the proof cylinder, computed from the data presented in Fig. 7 (a) using Eqtn. (4), and the CTE value determined from Fig. 7 (b) for all sample temperatures. All interaction strain values, e_{ii}, are clustered around zero strain, and exhibit no gradients with axial position at any temperature. The statistical scatter in the data, 3 ± 23 με in e_{11} and -8 ± 34 με in e_{22}, describe the accuracy and precision of the computations: since the sample is unconstrained, e_{ii} are expected to be zero.

The composite Figure 7 (d) depicts the variation of the boundary constraint term, B_C, at the measurement positions within the proof sample for all sample temperatures. The plotted values were computed from the data presented in Fig. 7 (a) using Eqtn. (5). These values show more scatter. However, we do not observe trends or gradients with axial position. The average boundary coefficient for all data in this plot is -6 ± 27 με. Since the sample is unconstrained, B_C terms are expected to be identically equal to zero.

In summary, the preliminary tests on both steel and Al proof specimens demonstrated that position-resolved values of thermal lattice strains, ε_{11}, ε_{22}, elastic interaction strains, e_{11}, e_{22},

and boundary coefficient values, B_C , obtained from neutron diffraction measurements, matched the predictions of the simple thermo-elastic analysis of the system formulated by Equations (2-5). The same formalism was, then, used for the composite specimen, where material parameters changed discontinuously across two interfaces.

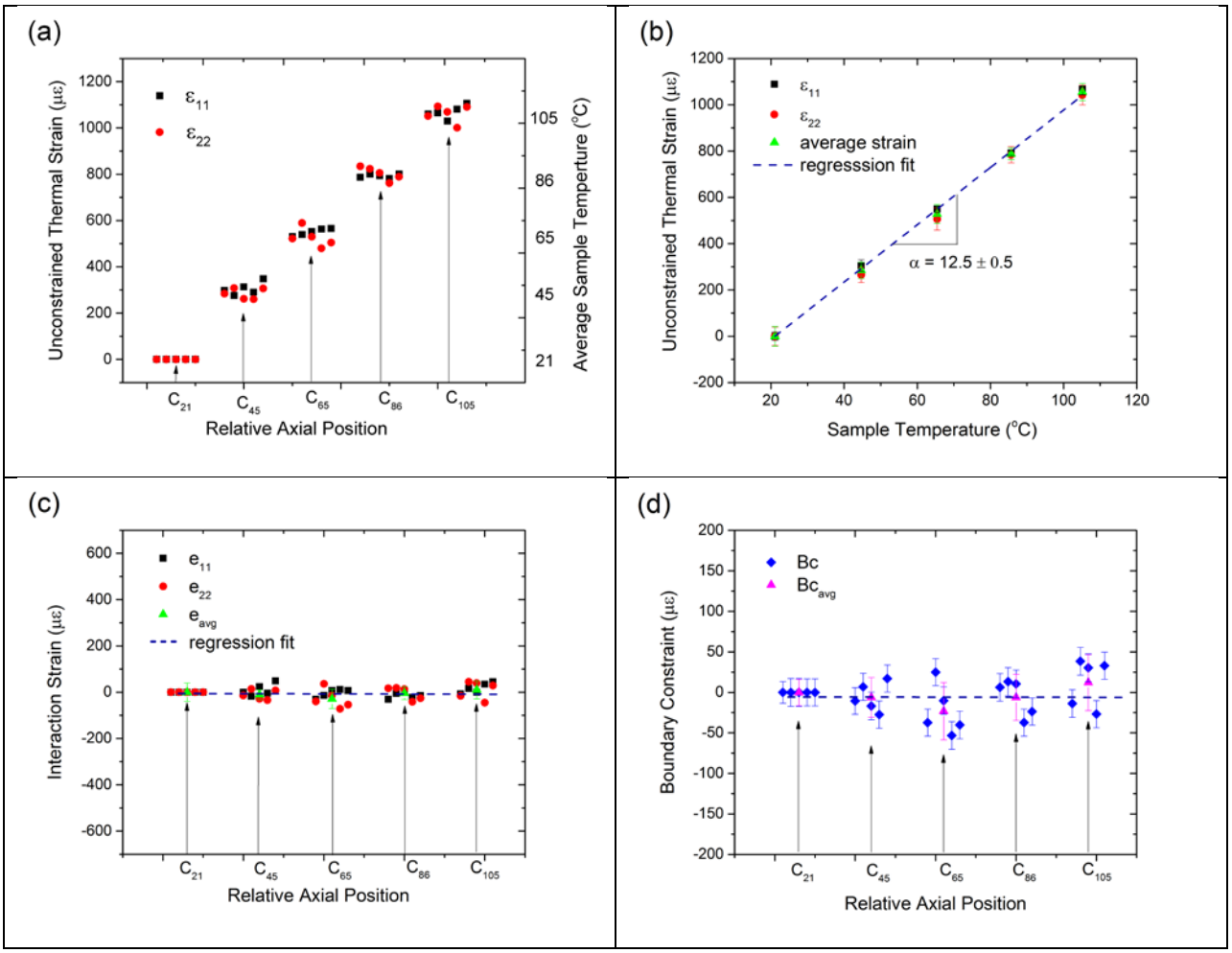

Fig. 7 (a) Spatial distribution of thermal lattice strains, $\boldsymbol{\varepsilon_{11}}$, $\boldsymbol{\varepsilon_{22}}$, within the central 50.8 mm of the steel proof specimen measured by neutron diffraction at five temperatures. The abscissa arrows indicate the center of the sample, $\boldsymbol{C_T}$, at each average sample temperature. The variation of average thermal lattice strains with average sample temperature is shown in plot (b). The slope of the regression line is the coefficient of thermal expansion. (c) Spatial distribution of interaction strains, $\boldsymbol{e_{11}}$, $\boldsymbol{e_{22}}$, within the central 50.8 mm of the steel proof specimen at five temperatures. The dashed line shows the regression line fitted to the average interaction strain, $\boldsymbol{e_{avg}}$ at each temperature. The boundary coefficient, $\boldsymbol{B_C}$, values computed from these data are plotted in (d), where the dashed line shows the regression line fitted to the average boundary coefficient value at each temperature. All error bars span ± 1 standard deviation.

.

Thermo-elastic Strain State of Composite Specimen

Figure 8 (a) shows the composite plot of lattice strains, $\varepsilon_{11}, \varepsilon_{22}$, measured by neutron diffraction from the steel-Al-steel composite cylinder which was heated to three set-point temperatures, RT, 60 and 100°C, under displacement control. These set points corresponded to average sample temperatures of 21, 53 and 85°C, respectively. The center of the specimen is marked for each temperature by 'C_T', where 'T' is the average temperature of the sample obtained from the seven embedded thermocouples. We observe that the lattice expands in both radial and axial directions in response to heating. However, due to the constraint provided by the load train boundaries, the total lattice strain is no longer isotropic.

Figure 8 (b) depicts the composite plot of interaction strain components, e_{11}, e_{22}, computed from the data shown in Fig. 8 (a) using Equation (4). Large, compressive, interaction strains in the axial direction result due to the displacement control of the load-train boundaries. The interaction strains in the transverse direction, e_{22}, are tensile due to Poisson expansion, and are lower in magnitude. We note that, in the unconstrained case, both e_{11} and e_{22}were zero within experimental error (Fig. 7 (c)).

Figure 8 (c) depicts a composite plot of the variation of the boundary constraint term, Bc, with position at the three temperatures. The term is identically zero at room temperature. At the higher temperatures the data is noisy due to the propagation of errors in the (measured) axial and transverse strain terms. Despite the noise, however, it is possible to see that the variation of Bc is not monotonic within error, which was the case for this term when computed for unconstrained thermal expansion (Fig. 7 (d)). Instead, we observe definite trends within each cylinder with several extrema, which are clearly out of error bounds. For example, we can identify three minima: points P_1, P_2 and P_3 , for the profile at 85°C, where P_1 , P_3 are in the left and right steel cylinders, respectively, bounding the interface. Point P_2, with Bc equal to zero (within experimental error), is located close to the middle of the Al cylinder, indicating uniaxial constraint at this position.

In summary, Figures 8 (a, b, c) show that a heterogeneous lattice strain state arises when the composite cylinder sample is heated uniformly under displacement control. This heterogeneity is due to the superposition of position-dependent elastic interaction strains on the thermal lattice strains. In addition, we observe finite values of the boundary constraint term, Bc, at multiple locations. Consequently, at certain locations within the composite sample the local constraint is not equivalent to the far-field uniaxial constraint imposed by displacement control of the mechanical tester. We used finite element analysis to investigate the strain/stress state within the system to explore further these results.

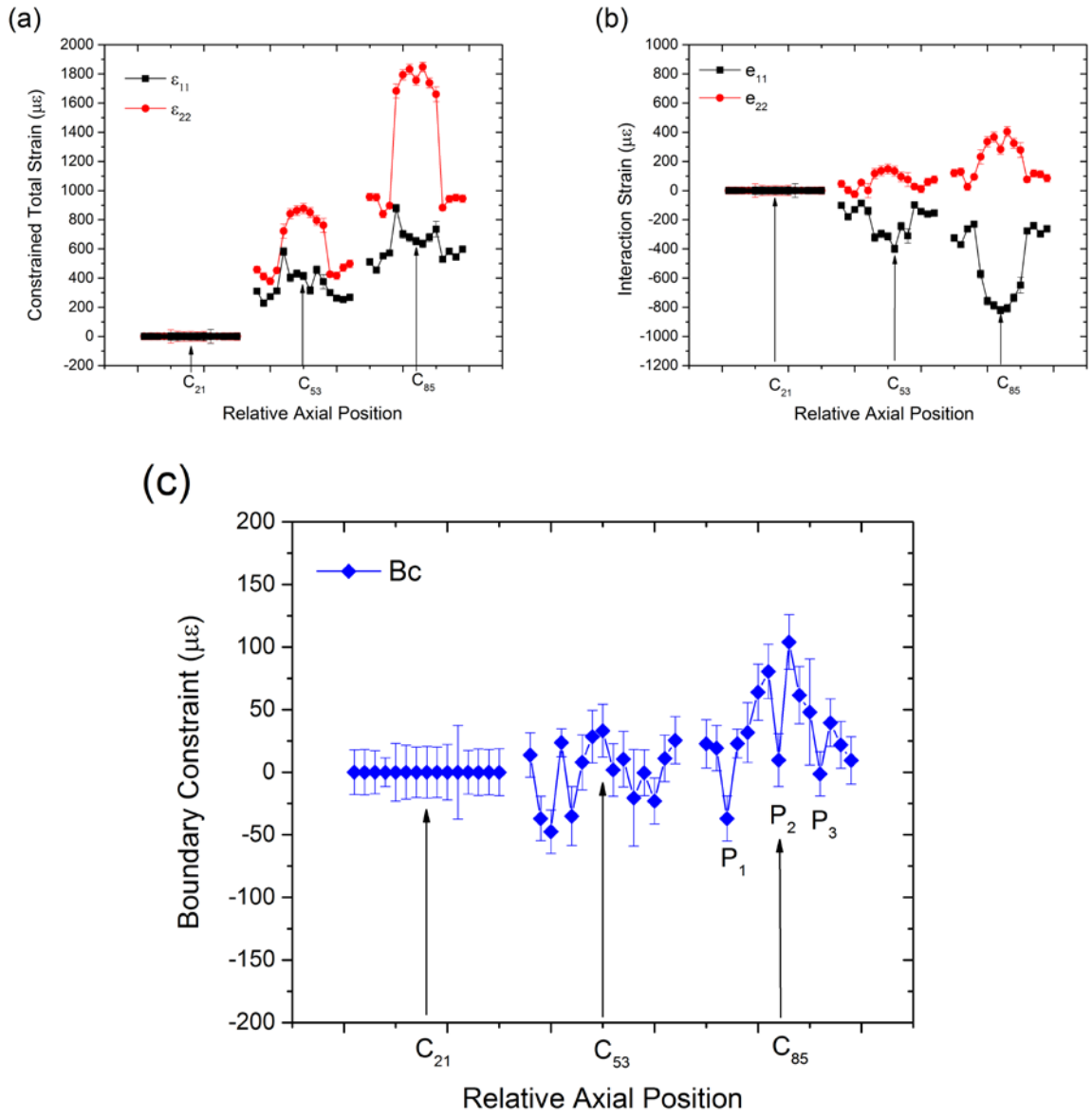

Fig. 8 (a) Spatial distribution of thermal lattice strains, $\boldsymbol{\varepsilon_{11}}$, $\boldsymbol{\varepsilon_{22}}$, within the central 68 mm of the composite specimen measured by neutron diffraction at three temperatures. The abscissa arrows indicate the center of the sample at each sample temperature, T. For each location, the corresponding interaction strains, $\boldsymbol{e_{11}}$, $\boldsymbol{e_{22}}$, (computed from Eqtn. (3)), and the boundary constraint term, $\boldsymbol{B_C}$,are plotted in (b), and (c) respectively. All error bars span ± 1 standard deviation.

Finite Element Modelling Results

The elastic interaction strains obtained from the composite specimen might contain contributions from: 1) the position-control constraint exerted by the load frame; and 2) the large mismatch in the coefficients of thermal expansion of the Al and steel cylinders which are in full mechanical contact across their cross-sections. Analysis of this second contribution using an analytical approach is non-trivial since one needs to formulate constitutive equations describing both interfaces.

While analysis of this problem using finite element modelling is easier, one still needs to specify the mechanical parameters and topologies associated with each boundary. Rather than assuming an arbitrary interface which yields modelling results that "fit" the experimental conditions, we assumed perfectly smooth cylinder surfaces in our models and computed the strain/stress distributions within these models for two types of interfaces.

First we specified fully-coupled cylinder interfaces with tie-constraints. For this case the transverse strains in the material volumes immediately adjoining the interfaces are forced to be compatible. For the second case the interfaces were assumed to be fully-uncoupled, such that the cylinders on both sides of the interfaces could radially expand without mutual hindrance. This corresponds to a friction-free state. For brevity we will report results for both cases from our model of the composite cylinder after it had been heated from room temperature to the higher measurement temperature (21 to 85˚C) in the position-control mode. We note that all FEM simulations yielded equal transverse strain terms, $\varepsilon_{22} = \varepsilon_{33},\ e_{22} = e_{33}$, for all locations.

Figures 9 (a, b) depict the variation of the total strains, $\varepsilon_{11}, \varepsilon_{22}$, along the composite cylinder axis when the steel-aluminum interfaces were specified as tie-constrained in the radial direction (Fig. 9 (a)) or completely unconnected (Fig. 9 (b)) in the finite element model. In the latter case, both the transverse and axial strain profiles at both interfaces can be approximated by Heaviside functions, indicating the negligible influence of the steel-aluminum interfaces on the distribution of applied strains. In contrast, the corresponding strain distributions for the fully-

coupled interface exhibit multiple extrema and inflection points in both the aluminum and steel cylinders. These effects are much more pronounced in the axial strain distribution. In the transverse direction the tie-constraint across the interface causes a smooth, continuous variation of the transverse strain across the interface.

Figures 9 (c, d) depict the variation of interaction strains, e_{11}, e_{22}, computed from the strain values shown in Fig. 9 (a, b) using Equation (4). Large, compressive, interaction strains in the axial direction, and tensile interaction strains of lower magnitude in the transverse direction, are observed for both completely-coupled and fully-uncoupled interface configurations. For the non-coupled interface, the variations of e_{11}, e_{22} across the interfaces can be represented by step functions (Fig. 9 (d)). When we specify fully-coupled interfaces between materials of different physical parameters, the variation of the interaction strains with axial position becomes non-monotonic for both longitudinal and transverse directions (Fig. 9 (c)).

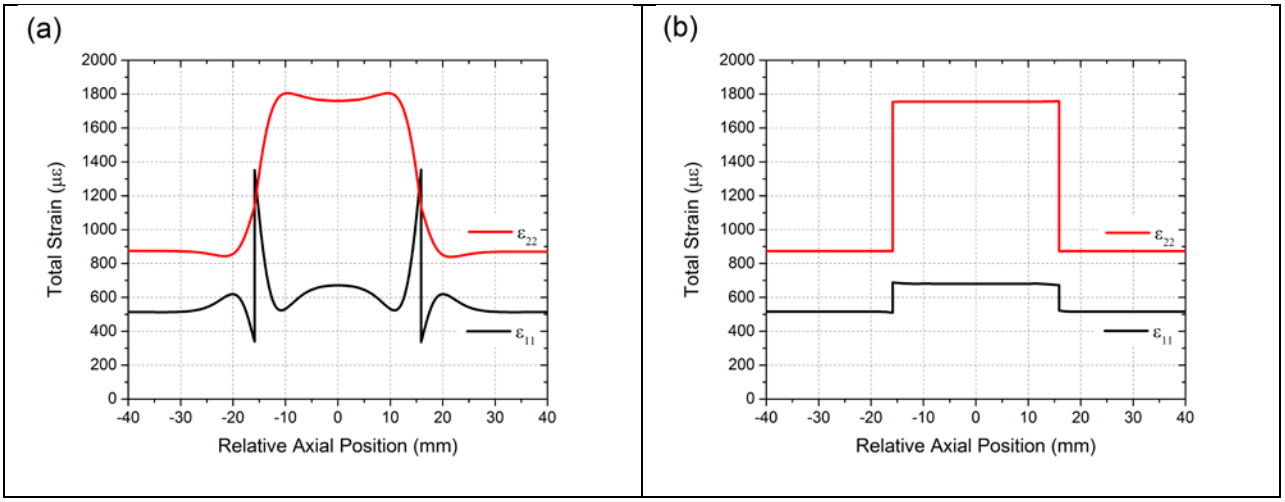

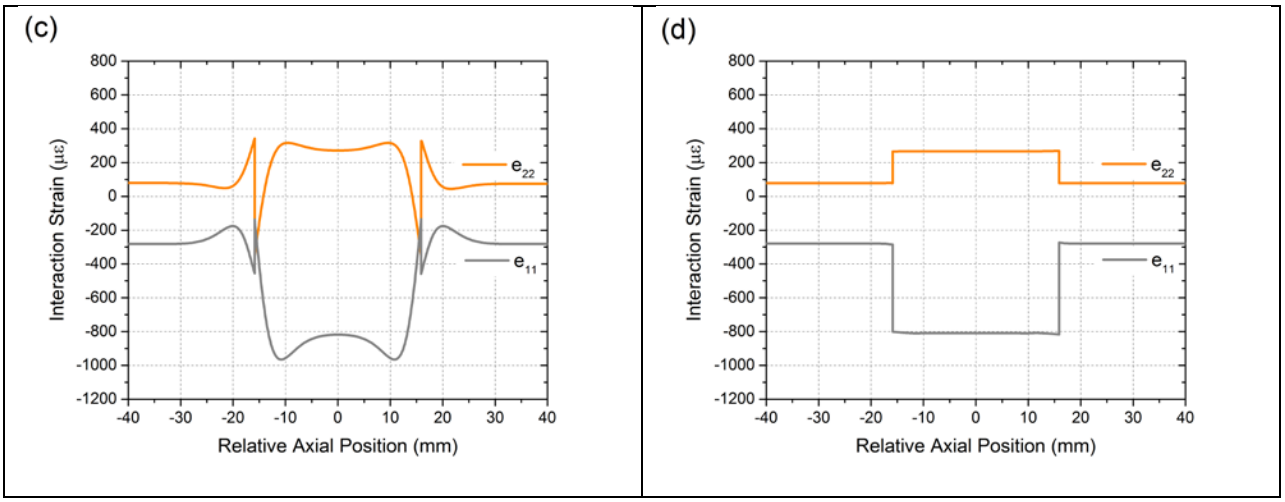

Fig. 9 (a-d) Variation of total axial and transverse strains (a, b), elastic interaction strains (c, d) with axial position obtained from the finite element model of the composite cylinder heated to 85˚C under displacement control for coupled (left) and friction-free (right) aluminum-steel interfaces, respectively.

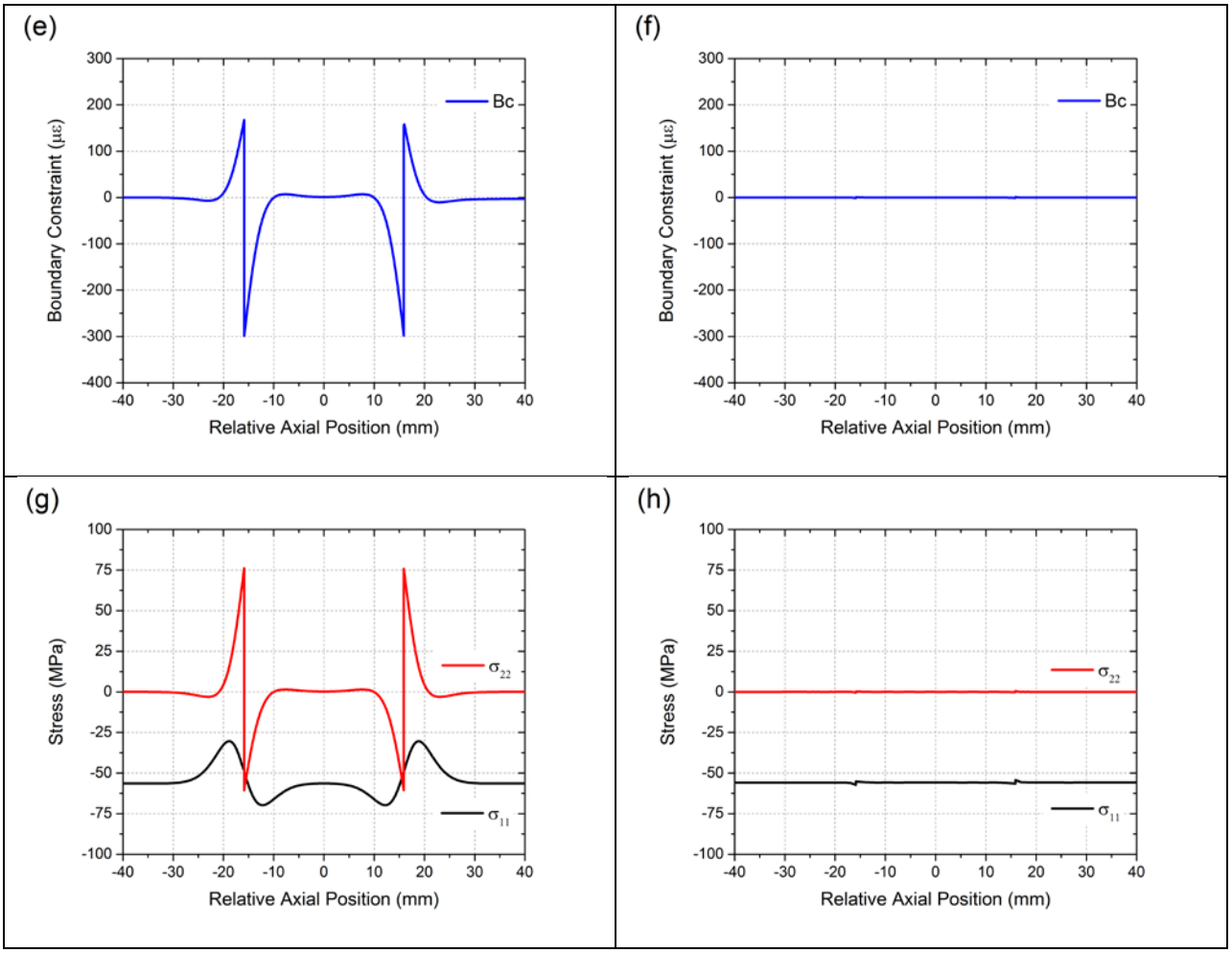

Fig. 9 (e-f) Variation of, boundary constraint coefficients (e, f), and axial and transverse stresses (g, h) with axial position obtained from the finite element model of the composite cylinder heated to 85˚C under displacement control for coupled (left) and friction-free (right) aluminum-steel interfaces, respectively.

Figures 9 (e, f) depict the longitudinal variation of the boundary constraint term, Bc, with position, computed from the data shown in Fig. 9 (a, b) using Equation (5) and the relevant constants shown in Table 1. The terms obtained from the model with uncoupled aluminum-steel interfaces are zero at all points along the axis (Fig. 9 (f)). This indicates that all of the reaction strains arising in response to constrained thermal expansion were linked by equations of isotropic elasticity; there were no contributions from the constraint of dissimilar materials in contact.

The variation of Bc with axial position for the fully-coupled steel-aluminum interfaces (Fig. 9 (e)) show extrema bracketing the interfaces. For this case Bc reaches zero only within the central segment of the Al cylinder. This observation indicates that the constraint effects of both coupled interfaces have decayed to negligible levels in this central region.

Finally, in Figures 9 (g, h) the variation of axial and transverse stresses, σ_{11}, σ_{22}, obtained from the finite element model are plotted. We observe that, for the friction-free case (Fig. 9 (h)), there is no transverse stress term. The axial stress term, σ_{11}, approximately -56 MPa, is independent of position. For the model with fully-coupled interfaces (Fig. 9 (g)), the radial boundary constraint causes finite stress values around the interfaces. These terms decay to zero in all cylinders with distance from the interfaces. The corresponding axial stress term, σ_{11}, tends to the far-field stress, -56 MPa, away from the interfaces, but oscillates around this value near them.

Comparison of Strain States from Modelling and Measurement

Since diffraction data directly yield particular strain tensor components through Eqtn. (1), we first compared the strain components predicted by the finite element model (Fig. 9) with the values obtained from neutron diffraction measurements at 85°C. (Fig. 8). In Figure 10 the experimentally determined parameters are plotted with the FEM results for ease of comparison.

Figure 10 (a) shows that, for the neutron-diffraction accessible regions of the composite

cylinder[7], the measured transverse strain components, ε_{22}, are quite close to the FEM results for both fully-coupled and friction-free interfaces. On the other hand the axial strains, ε_{11}, at the same locations (measured simultaneously using a different bank of detectors) are, within error, different from the predictions of these models. These differences decrease with distance from the interfaces. The slight asymmetry in strain results is due to a slightly lower temperature distribution (Figure 10 (d)). In the steel cylinders, axial and transverse lattice strains, ε_{11}, ε_{22}, show acceptable agreement with the model predictions close to the interface. Away from the interfaces the transverse strains, ε_{22}, are slightly higher (~5 %) than the model predictions. The differences are slightly larger than measurement error. These differences might be caused by the radial expansion constraint at the steel-aluminum spacer interfaces.

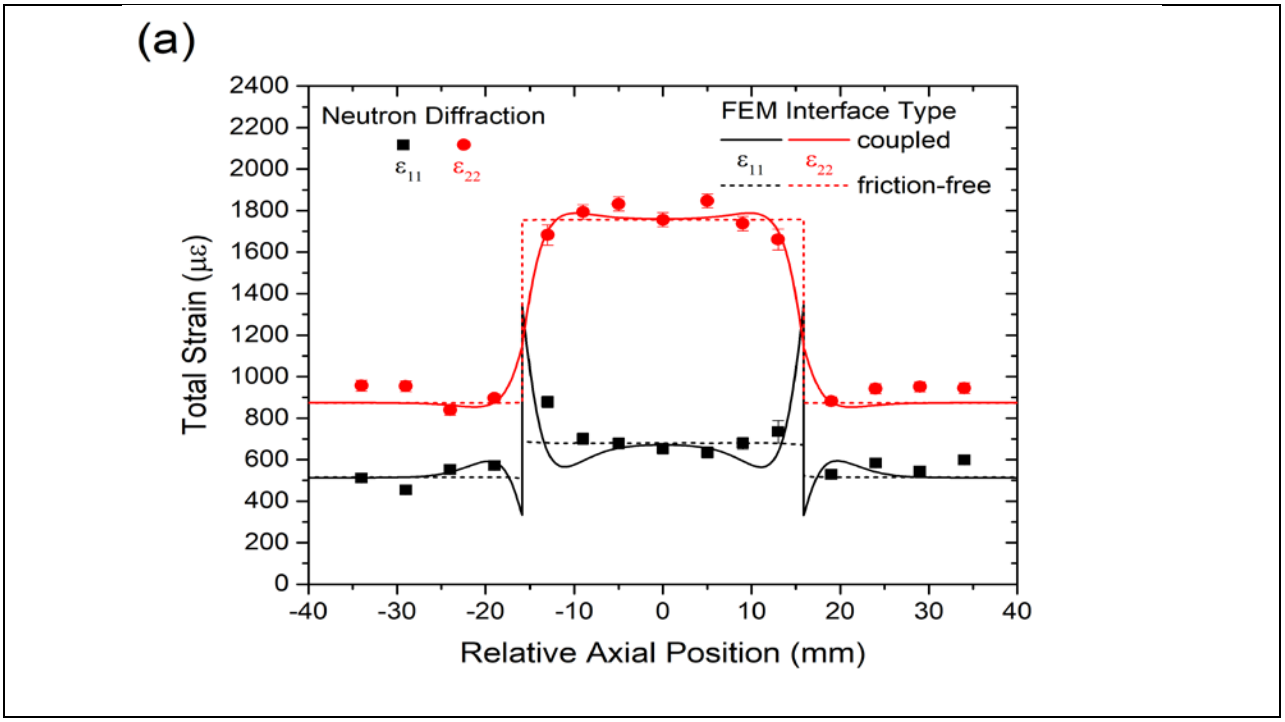

[7] We note that the steel and aluminum material volumes immediately bordering both interfaces-and containing the steep interaction strain gradients- could not be interrogated using neutron diffraction due to possible positioning errors and the attendant "unfilled gage volume" issues [35].

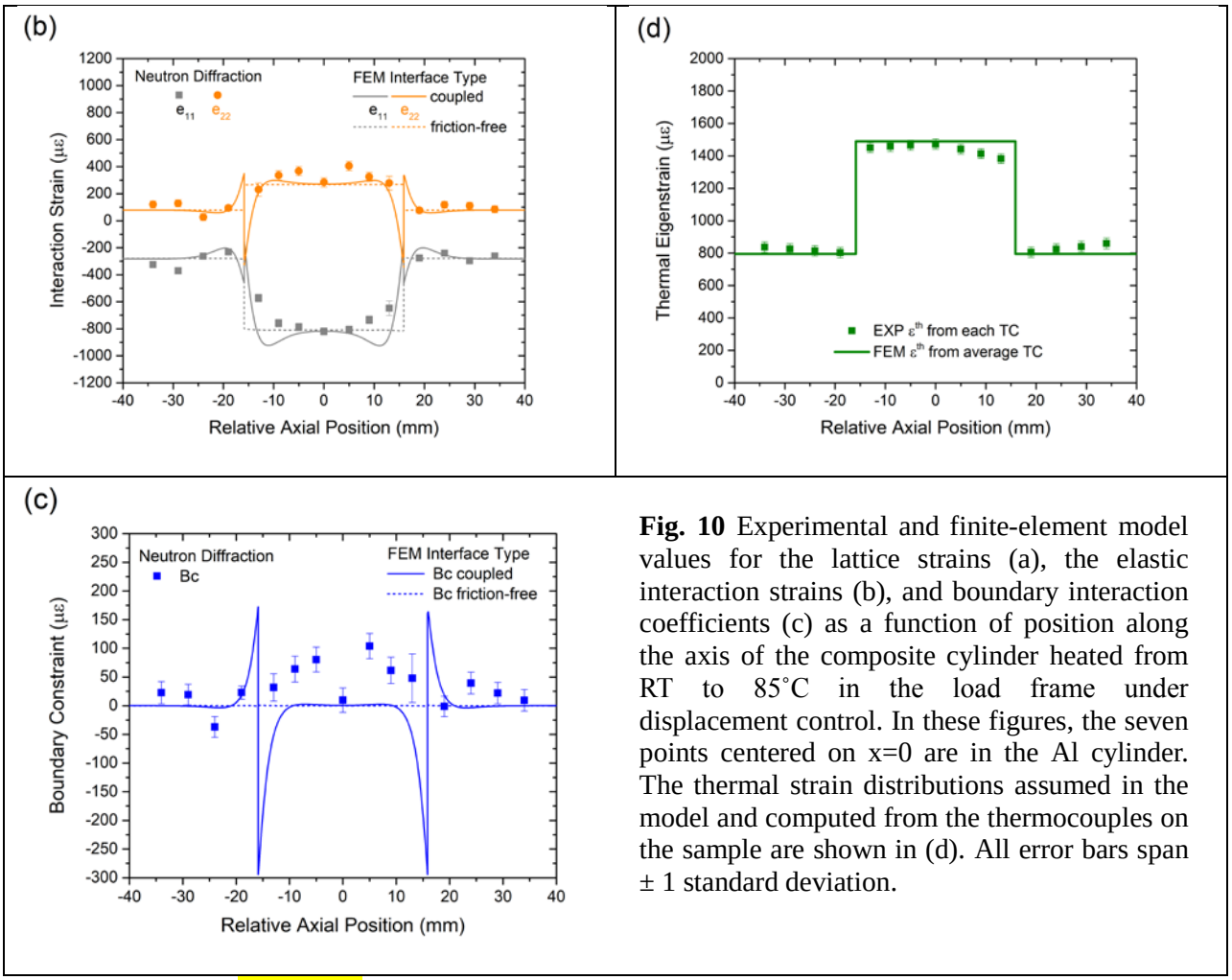

Fig. 10 Experimental and finite-element model values for the lattice strains (a), the elastic interaction strains (b), and boundary interaction coefficients (c) as a function of position along the axis of the composite cylinder heated from RT to 85˚C in the load frame under displacement control. In these figures, the seven points centered on x=0 are in the Al cylinder. The thermal strain distributions assumed in the model and computed from the thermocouples on the sample are shown in (d). All error bars span ± 1 standard deviation.

The axial and transverse interaction strains, e_{11}, e_{22}, computed using Eqtn. (4) from the measured lattice strain components plotted in Fig. 10 (a) are depicted in Figure 10 (b). In the aluminum cylinder, the axial interaction strains, e_{11}, exhibit symmetric maxima, approximately -580 με, close to the interfaces and decay smoothly to an asymptotic value, approximately -800 με, towards the center of the cylinder. This asymptotic value matches, within error, the predictions of the FEM simulations. However, we observe significant differences, around 300 and 100 με respectively, between the measured and modelling values closer to the interfaces. In comparison, the experimental e_{11}values for the proof cylinder showed no trends (Figure 7 (c)), and their average value was 3 ± 23 με.

The experimental values of the transverse interaction strains, e_{22}, are also symmetric around the center of the aluminum cylinder. For this component, however, the maximum deviation

between the experimental and modelled values, approximately 150 με, are at axial positions -5 and +5 mm, respectively. The deviation decreases closer to the interfaces. In addition, there is good agreement between experimental and modelled e_{22}values at the center of the cylinder. We note that, for the proof cylinder, the radial interaction terms also did not show any axial dependency. The average experimental e_{22} for this case was -8 ± 34 με.

The interaction terms, e_{11}, e_{22}, together, agree with the model predictions only at the center of the Al cylinder. At other locations such (simultaneous) agreement is not observed. We used the boundary interaction coefficient, *Bc* (Eqtn. (5)), which is a function of both e_{11} and e_{22} , to determine the axial positions where the experimental and modelled strain tensors agree. Figure 10 (c) depicts the variation of *Bc* along the cylinder axis. The distribution of the experimental Bc parameter with position is symmetric, within measurement error, around the specimen center. For axial positions between x= -12 and +12 mm, both finite element models (with free or fully-coupled interfaces) predicted $Bc = 0$. However, within this range the experimental boundary coefficient was zero only at the sample center (x=0), indicating that approximately the 10% volume of the aluminum cylinder at the center was under the expected uniaxial constraint. For all other locations sampled by neutron diffraction the experimental Bc values are observed finite and greater than zero.

In summary, while the total lattice strains, ε_{11}, ε_{22} , and interaction strains, e_{11}, e_{22}, show various regions of agreement with the FEM predictions within the Al cylinder (Figures 10 (a, b)), the boundary coefficient, Bc, values show large, systematic, deviations from the model values for most of the cylinder. Given the derivation of Eqtn. (5), this observation simply indicates that these regions (with non-zero Bc) are not experiencing the expected uniaxial constraint by the load frame in response to thermal expansion. The actual strain distribution will depend on the effective geometries of the interfaces and the local load distribution. Since we have experimental strain data only along longitudinal and one transverse directions, we cannot determine the full strain tensor at these locations and determine the exact nature of the constraint.

Comparison of Stress States from Modelling and Measurement

The eigenstrain method directly provides the position-resolved stress distribution in the composite cylinder by using numerical modelling which takes the thermal expansion eigenstrains and the boundary conditions imposed by the load frame in displacement control as its input. With neutron data stresses at each measurement location corresponding to the measured strains must be computed from the interaction strain data, e_{11}, e_{22}, obtained from neutron diffraction (Fig. 10 (b)) using the isotropic form of Hooke's law:

$$\sigma_{ii} = \frac{E}{(1+\nu)} e_{ii} + \frac{\nu E}{(1+\nu)(1-2\nu)} e_{kk} \qquad (6)$$

If we utilize the ideal macroscopic (cylindrical) symmetry of the system[8], the transverse interaction strains, e_{22}, e_{33} can be considered equal. Consequently, the trace of the interaction strain tensor, e_{kk}, becomes $e_{kk} = e_{11} + 2e_{22}$, resulting in equal transverse stress terms, $\sigma_{22} = \sigma_{33}$.

Figure 11 (a) shows the variation of axial and transverse stresses along the cylinder axis computed from Equation (6) using the neutron diffraction data, and obtained from the eigenstrain method. Both fully-coupled and friction-free interface results are included. The bold dashed-line marks the far-field stress, imposed by the load frame on the sample grips to maintain constant displacement in response to the thermal expansion of the composite cylinder sample upon being heated from room temperature to 85˚C.

The axial stress, σ_{11}, obtained from the eigenstrain method assuming friction-free steel-aluminum interfaces (the thin dashed line at -56 MPa) shows excellent agreement with the far-field stress applied by the load frame (thick dashed line at -58 MPa) in the entire sample volume. The axial stress values obtained from neutron diffraction analysis and the eigenstrain method with fully-coupled cylinder interfaces oscillate around the applied far-field stress near the aluminum-steel interfaces, and tend towards the far-field stress from the load frame at positions distant from the interfaces. The oscillations cancel out, within error, if the stress values are integrated over the sampled composite volume; this computation yields $\sigma_{11} = -49 \pm 10$ and $\sigma_{22} = 8 \pm 9$ MPa, which approximate the expected far-field values, -58 MPa and 0 MPa,

[8] Based on the axial distribution of the boundary interaction coefficients, $Bc(x)$, (Figure 10 (c)) this might be a weak assumption.

respectively. However, the forms of the axial and transverse stress distributions do not match the eigenstrain predictions.

This point is better illustrated in Figure 11 (b), where the traces of the stress tensors, σ_{kk}, for the experimental results and the two eigenstrain simulations are shown. We observe that the experimental data do not lie between the model predictions of the two extreme cases (fully-coupled and friction-free) assumed for the cylinder interfaces, and have a significantly different distribution.

(a)

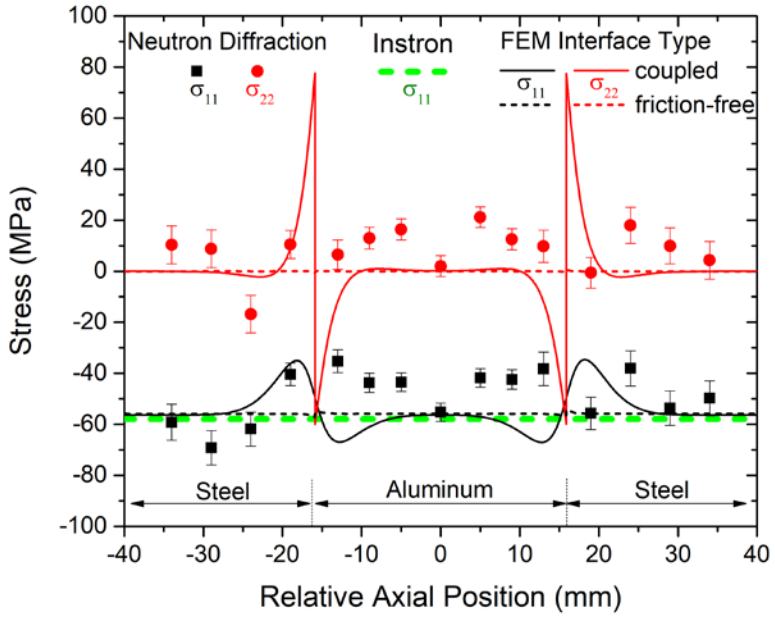

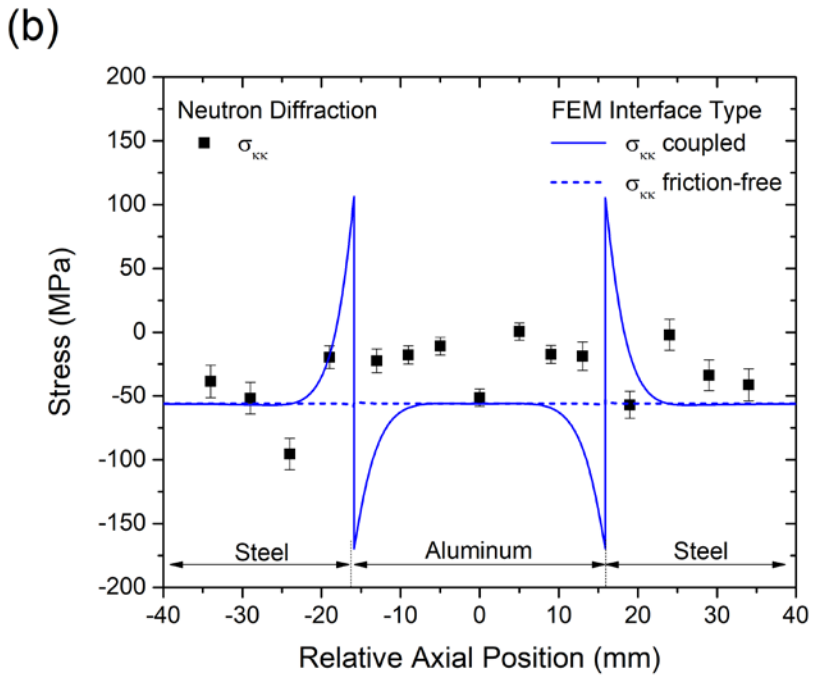

Fig. 11 Variation of axial and transverse stresses, σ_{11}, σ_{22} , along the cylinder axis computed from Equation (6), and obtained from finite element modelling assuming fully-coupled and friction-free aluminum steel interfaces. The solid line marks the far-field stress, imposed by the load frame (a). The variations of the corresponding stress tensor traces, σ_{kk}, are plotted in (b). In these plots the Al/Fe interfaces are at ±15.9 mm. All error bars span ± 1 standard deviation.

Discussion and Conclusions

Our results support Luzin's conclusion [21] that the eigenstrain approach can provide unique and tractable only for simple geometries (such as cylinders) when the eigenstrain distributions, also, have simple functional forms. The computed and modelled thermal eigenstrains showed excellent agreement with lattice strains obtained from the neutron diffraction results for the (homogeneous) proof specimens of steel and aluminum. In these specimens, the eigenstrain distribution was homogeneous and continuous within the specimen volume. The validated eigenstrains were used to determine the thermoeleastic response of a composite cylinder, consisting of an aluminum cylinder sandwiched between two steel cylinders of the same diameter, which was heated *in situ* on a neutron-diffractometer under displacement control (fixed grip positions). In this case, some measured lattice strains showed significant deviations from the

finite element modelling results near the material interfaces even though the exact (calculated/measured) eigenstrains were specified for each particular cylinder within the models. We attribute the discrepancies to the specification of the interfaces: since we did not know the exact geometry and friction coefficients of these interfaces, we assumed that the interfaces were either ideally friction-free, or fully-coupled. When we compared the FEM results from both simulations to the measured axial and transverse lattice strains in the aluminum cylinder, we observed that, while there were regions where either axial or transverse strains agreed quite well with FEM results, there was only one region, right at the center of the specimen, where the ideal strain state predicted by both models agreed with the measured strain state; the strain state distributions within the aluminum cylinder closer to the interfaces were not captured by either model. The experimental results also showed that the measured interaction profiles did not fall, as we expected, between the results of our numerical models with friction-free and fully-coupled interfaces. This issue is under further investigation and will be reported in a future publication.

We observed worse agreement between the axial and transverse stress values computed from the experimentally determined strain components and the values predicted by the FEM models. While both stress components agreed with the model predictions at the middle of the aluminum cylinder, and far away from the interfaces in both steel specimens, the experimental values differed in form and magnitude in most regions. Such discrepancies might be due to our assumption of perfect radial symmetry in calculating the stress values from experimental strain components. While the overall sample/load-train geometry is macroscopically radially symmetric, the relatively compliant configuration of the load frame, coupled with specimen machining tolerances which define the actual contact geometries of the steel-aluminum interfaces, might result in deviations from perfect radial symmetry, giving rise to the observed deviations. On the other hand, during routine implementations of the eigenstrain method, macroscopic symmetry specifications are used in the FEM models in addition to the eigenstrain values from proof specimens. This illustrates the “inverse-problem” nature of the eigenstrain method. To obtain a unique and correct solution, one needs to specify many parameters within the specimen, at both macro and micro scales, in addition to eigenstrains. If this is not properly done, the results might be erroneous. On the other hand, the experimental determination and verification of these parameters will offset the efficiency claimed for the eigenstrain method,

since the major advantage claimed for this approach is the ability to calculate the entire residual stress field within an actual engineering component from a limited set of (experimental) residual stress data.

The current results also intimate that, virtual interfaces[9] within a quasi-homogeneous solid, formed through a heterogeneous distribution of eigenstrains, can introduce elastic strain gradients within the material which cannot be predicted *a priori* in a quantitative manner. For example, the plastic strain distribution within a sphere plastically deformed between parallel platens will show regions with very different plastic strains in close proximity; the form and extent of these domains depend on the hardness and smoothness of the platens, the presence and characteristics of any lubricating film between the platen surfaces and the sphere, and the rate of deformation; a rigorous analytical description of the eigenstrain distribution is not possible without full experimental analysis of the exact geometry. In this case, the local plastic strain distribution is not a continuous monotonic function of the overall plastic strain computed from the irreversible change in sphere diameter (Noyan, 1988) [39]. The situation in this case is analogous to the mechanically constrained interfaces in the composite cylinder sample used in our current study. In both cases, the exact local elastic strain distribution, arising in response to the heterogeneous eigenstrain deformation, cannot be correctly predicted only from studies of samples with uniform deformation profiles.

Summary

The effects of internal boundaries on the accuracy of residual stress values obtained from the eigenstrain method have been explored experimentally and through finite-element modeling of a composite specimen consisting of an aluminum cylinder sandwiched between steel cylinders of the same diameter. The specimen was uniformly heated while it was constrained *in situ* on a load frame mounted on the SMARTS engineering neutron diffractometer. We observed that the simple eigenstrain method predicted sharp transitions in strain at the boundaries of the aluminum and

[9] A virtual interface in a quasi-homogeneous solid such as a polycrystalline sample larger than the representative volume, delineates regions of different hardness, yield stress, grain size, texture, etc. formed through heterogeneous plastic flow caused by boundary conditions. An example can be seen in reference [40].

steel elements within the composite sample which were not replicated in the experimental results. To properly account for frictional effects at interfaces, specification of precise interface parameters, such as friction coefficients and surface roughness, are needed. It might not always be possible to obtain such parameters.

Our results show that:

1. The eigenstrain method of residual stress determination cannot be applied in a simple, straightforward, manner to samples with real or virtual interfaces where abrupt eigenstrain gradients can form. While it might be possible to use complicated models with “fitting parameters” which yield better agreement between measured and modelled lattice strains, the results cannot be extrapolated to other geometries with confidence.
2. The general eigenstrain method should be used with care in systems which have abrupt changes in cross-section, buried interfaces, or other features, which cause local constraint effects.

In summary, further characterization, validation and verification studies are needed before this new technique can be generally applied with confidence to mission-critical systems.

Acknowledgements This research effort was sponsored by the Air Force Research Laboratory, Aerospace Systems Directorate, under contracts FA8650-10-D-3037 and FA8650-12-D-3212, and has benefited from the use of the Lujan Neutron Scattering Center at LANSCE. Los Alamos National Laboratory is operated by Los Alamos National Security LLC under DOE Contract DE-AC52-06NA25396. MEF is grateful for funding from the Lloyd’s Register Foundation, a charitable foundation helping to protect life and property by supporting engineering-related education, public engagement and the application of research.

References

[1] Mura, T., 1987. Micromechanics of Defects in Solids, 2nd ed. Martinus Nijhoff Publishers, Dordrecht, Netherlands.

[2] Reissner, H., 1931. Eigenspannungen und Eigenspannungsquellen. Zeitschrift Fur Angewandte Mathematik und Mechanik 11, 1-8.

[3] Eshelby, J.D., 1957. The Determination of the Elastic Field of an Ellipsoidal Inclusion, And Related Problems. Proceedings of the Royal Society of London Series a-Mathematical and Physical Sciences 241, 376-396.

[4] Eshelby, J.D., 1959. The Elastic Field outside an Ellipsoidal Inclusion. Proceedings of the Royal Society of London Series a-Mathematical and Physical Sciences 252, 561-569.

[5] Fujimoto, T., 1970. A Method for Analysis of Residual Welding Stresses and Deformations Based on the Inherent Strain - A Theoretical Study of Residual Welding Stresses and Deformations (Report 1). Journal of the Japan Welding Society 39, 236-252.

[6] Ueda, Y., Fukuda, K., Nakacho, K., Endo, S., 1975. A New Measuring Method of Residual Stresses with the Aid of Finite Element Method and Reliability of Estimated Values. Transactions of Japan Welding Research Institute 4, 123-131.

[7] Hill, M.R., Nelson, D.V., 1995. The Inherent Strain Method for Residual Stress Determination and Its Application to a Long Welded Joint. ASME-PUBLICATIONS-PVP 318, 343-352.

[8] Hill, M.R., Nelson, D.V., 1998. The Localized Eigenstrain Method for Determination of Triaxial Residual Stress in Welds. ASME-PUBLICATIONS-PVP 373, 397-404.

[9] Luckhoo, H.T., Jun, T.S., Korsunsky, A.M., 2009. Inverse Eigenstrain Analysis of Residual Stresses in Friction Stir Welds. Procedia Engineering (Mesomechanics 2009) 1, 213-216.

[10] Jun, T.S., Dragnevski, K., Korsunsky, A.M., 2010. Microstructure, Residual Strain, and Eigenstrain Analysis of Dissimilar Friction Stir Welds. Mater. Des. 31, S121-S125.

[11] Korsunsky, A.M., 2005. On The Modelling of Residual Stresses due to Surface Peening Using Eigenstrain Distributions. J. Strain Anal. Eng. Des. 40, 817-824.

[12] Jun, T.S., Venter, A.M., Korsunsky, A.M., 2011. Inverse Eigenstrain Analysis of the Effect of Non-uniform Sample Shape on the Residual Stress Due to Shot Peening. Exp. Mech. 51, 165-174.

[13] Song, X., Liu, W.C., Belnoue, J.P., Dong, J., Wu, G.H., Ding, W.J., Kimber, S.A.J., Buslaps, T., Lunt, A.J.G., Korsunsky, A.M., 2012. An Eigenstrain-Based Finite Element Model and the Evolution of Shot Peening Residual Stresses During Fatigue of GW103 Magnesium Alloy. Int. J. Fatigue 42, 284-295.

[14] Korsunsky, A.M., 2006. Residual Elastic Strain Due to Laser Shock Peening: Modelling by Eigenstrain Distribution. J. Strain Anal. Eng. Des. 41, 195-204.

[15] Achintha, M., Nowell, D., 2011. Eigenstrain Modelling of Residual Stresses Generated by Laser Shock Peening. J. Mater. Process. Technol. 211, 1091-1101.

[16] Hu, Y.X., Grandhi, R.V., 2012. Efficient Numerical Prediction of Residual Stress and Deformation for Large-Scale Laser Shock Processing Using the Eigenstrain Methodology. Surf. Coat. Technol. 206, 3374-3385.

[17] Achintha, M., Nowell, D., Shapiro, K., Withers, P.J., 2013. Eigenstrain Modelling of Residual Stress Generated by Arrays of Laser Shock Peening Shots and Determination of the Complete Stress Field Using Limited Strain Measurements. Surf. Coat. Technol. 216, 68-77.

[18] Correa, C., Gil-Santos, A., Porro, J.A., Diaz, M., Ocana, J.L., 2015. Eigenstrain Simulation of Residual Stresses Induced by Laser Shock Processing in a Ti6Al4V Hip Replacement. Mater. Des. 79, 106-114.

[19] Coratella, S., Sticchi, M., Toparli, M.B., Fitzpatrick, M.E., Kashaev, N., 2015. Application of the Eigenstrain Approach to Predict the Residual Stress Distribution in Laser Shock Peened AA7050-T7451 Samples. Surf. Coat. Technol. 273, 39-49.

[20] Jun, T.S., Korsunsky, A.M., 2010. Evaluation of Residual Stresses and Strains Using the Eigenstrain Reconstruction Method. Int. J. Solids Struct. 47, 1678-1686.

[21] Luzin, V., 2014. Use of the Eigenstrain Concept for Residual Stress Analysis. Materials Science Forum (International Conference on Residual Stresses 9) 768-769, 193-200.

[22] Noyan, I.C., Cohen, J.B., 1985. An X-Ray-Diffraction Study of the Residual-Stress Strain Distributions In Shot-Peened 2-Phase Brass. Materials Science and Engineering 75, 179-193.

[23] Noyan, I.C., Cohen, J.B., 1987. Residual Stress: Measurement by Diffraction and Interpretation. Springer.

[24] Schajer, G.S., 1988. Measurement of Non-uniform Residual-stresses using the Hole-drilling method .1. Stress Calculation Procedures. J. Eng. Mater. Technol.-Trans. ASME 110, 338-343.

[25] Schajer, G.S., 1988. Measurement of Non-uniform Residual-stresses using the Hole-drilling method .2. Practical Application of the Integral method. J. Eng. Mater. Technol.-Trans. ASME 110, 344-349.

[26] Prime, M.B., 2001. Cross-Sectional Mapping of Residual Stresses by Measuring the Surface Contour after a Cut. J. Eng. Mater. Technol.-Trans. ASME 123, 162-168.

[27] Prime, M.B., Gnaupel-Herold, T., Baumann, J.A., Lederich, R.J., Bowden, D.M., Sebring, R.J., 2006. Residual Stress Measurements in a Thick, Dissimilar Aluminum Alloy Friction Stir Weld. Acta Mater. 54, 4013-4021.

[28] Schajer, G.S., 2010. Relaxation Methods for Measuring Residual Stresses: Techniques and Opportunities. Exp. Mech. 50, 1117-1127.

[29] Woo, W., An, G.B., Kingston, E.J., DeWaldd, A.T., Smith, D.J., Hill, M.R., 2013. Through-Thickness Distributions of Residual Stresses in Two Extreme Heat-Input Thick Welds: A Neutron Diffraction, Contour Method and Deep Hole Drilling Study. Acta Mater. 61, 3564-3574.

[30] Metals Handbook, 1990, Vol.1 - Properties and Selection: Irons, Steels, and High-Performance Alloys, ASM International 10th Ed.

[31] Metals Handbook, 1990, Vol.2 - Properties and Selection: Nonferrous Alloys and Special-Purpose Materials, ASM International 10th Ed.

[32] http://www.matweb.com/search/datasheet.aspx?matguid=848bdecf89b74ef986925162e6a6255e&ckck=1

[33] Noyan, I.C., Brügger, A., Betti, R., Clausen, B., 2010. Measurement of Strain/Load Transfer in Parallel Seven-wire Strands with Neutron Diffraction. Exp. Mech. 50, 265-272.

[34] Lee, S.Y., Skorpenske, H., Stoica, A.D., An, K., Wang, X.L., Noyan, I.C., 2014. Measurement of Interface Thermal Resistance with Neutron Diffraction. Journal of Heat Transfer-Transactions of the ASME 136.

[35] Spooner, S., Wang, X.L., 1997. Diffraction Peak Displacement in Residual Stress Samples due to Partial Burial of the Sampling Volume. Journal of Applied Crystallography 30, 449-455.

[36] Vondreele, R.B., Jorgensen, J.D., Windsor, C.G., 1982. Rietveld Refinement with Spallation Neutron Powder Diffraction Data. Journal of Applied Crystallography 15, 581-589.

[37] Clausen, B., 2004. SMARTSware Manual. LA-UR 04-6581, Los Alamos, NM, USA: Los Alamos National Laboratory.

[38] Mei, F., Noyan, I.C., Brügger, A., Betti, R., Clausen, B., Brown, D., Sisneros, T., 2013. Neutron Diffraction Measurement of Stress Redistribution in Parallel Seven-Wire Strands after Local Fracture. Exp. Mech. 53, 183-193.

[39] Brügger, A., Lee, S.-Y., Mills, J. A. A., R. Betti, Noyan, I.C., 2017, Partitioning of Clamping Strains in a Nineteen Parallel Wire Strand, Exp. Mech. 57, 921-937.

[40] Noyan, I.C., 1988. Plastic Deformation of Solid Spheres. Philos. Mag. A-Phys. Condens. Matter Struct. Defect Mech. Prop. 57, 127-141.